

## Prospects of cooling a mechanical resonator with a transmon qubit in c-QED setup

Sourav Majumder, Tanmoy Bera, and Vibhor Singh<sup>\*</sup>

*Department of Physics, Indian Institute of Science, Bangalore 560012, India*



(Received 13 June 2022; accepted 10 August 2022; published 23 September 2022)

Hybrid devices based on the superconducting qubits have emerged as a promising platform for controlling the quantum states of macroscopic resonators. The nonlinearity added by a qubit can be a valuable resource for such control. Here we study a hybrid system consisting of a mechanical resonator longitudinally coupled to a transmon qubit. The qubit readout can be done by coupling to a readout mode like in c-QED setup. The coupling between the mechanical resonator and transmon qubit can be implemented by the modulation of the superconducting quantum interference device inductance. In such a tripartite system, we analyze the steady-state occupation of the mechanical mode when all three modes are dispersively coupled. We use the quantum noise and the Lindblad formalism to show that the sideband cooling of the mechanical mode to its ground state is achievable. We further experimentally demonstrate that measurements of the thermomechanical motion are possible in the dispersive limit, while maintaining a large coupling between qubit and mechanical mode. Our theoretical calculations suggest that single-photon strong coupling is within the experimental reach in such hybrid devices.

DOI: [10.1103/PhysRevResearch.4.033232](https://doi.org/10.1103/PhysRevResearch.4.033232)

### I. INTRODUCTION

Control over the quantum states of a mechanical resonator by coupling them to optical modes can have several potential applications in the field of quantum technologies [1]. The traditional cavity-optomechanics based approach of coupling a mechanical resonator to an optical mode via the radiation-pressure interaction has been quite successful [2–9]. While the radiation-pressure mediated coupling in such devices is nonlinear, its magnitude is usually small in most implementations. Further, due to the dispersive interaction, the effects originating from the Kerr term are strongly suppressed [10,11].

To mitigate the limitations of linear cavity optomechanics, hybrid devices based on the strong nonlinearity of qubits have been proposed and developed [12–14]. These proposals explore their performance from the sideband cooling of the mechanical resonator [15] to the matter interferometry [16], while considering a wide range of two-level systems such as superconducting qubits [15,17–22], quantum dots [23], and nitrogen-vacancy defects in diamond [24]. Particularly, in the microwave domain, experimental realization of several hybrid devices has been shown using the nonlinearity of a superconducting qubit [25], Josephson capacitance [26,27], Josephson inductance [28–31], and piezoelectricity [32,33].

Among these different schemes, the electromechanical coupling stems from charge or flux modulation, and its tunability is controlled by the external parameters. Recently,

the magnetic flux-mediated coupling approach have shown promising experimental results [28]. These systems have demonstrated large electromechanical coupling [29–31], four-wave cooling of the mechanical resonator to near the quantum ground state [34], and Lorentz-force induced backaction on the mechanical resonator [35].

Motivated by the progress on the flux-mediated approach, here we investigate a coupled three-mode system consisting of a mechanical mode, transmon qubit, and a readout cavity. From the practical point of view, the additional readout cavity is a useful ingredient to consider as it allows the quantum non-demolition measurement of qubit mode in circuit-QED setup [36,37]. While a mechanical mode coupled to a two-level system has been studied extensively in the past [12,15,17,38,39], the focus of our investigation has been on treating the transmon qubit as a weakly anharmonic oscillator. In addition, we theoretically and experimentally address the readout of the mechanical mode when the transmon is detuned far away from the readout cavity. This regime is particularly important as large electromechanical coupling with the qubit mode can be achieved. Using the quantum-Langevin equation of motion [40] and Lindblad formalism [41], we analyze the possibility of sideband cooling of the mechanical resonator. Experimentally, we use a two-tone method to measure the thermomechanical motion, and compare it with analytical results.

This paper is organized as follows: In Sec. II, we discuss the theoretical model of the three coupled modes. We solve the system's equations of motion in Sec. III. The analytical solution of the system is analyzed in Sec. IV, where we have shown the possibility of cooling the mechanical resonator. In Sec. V, we show experimental and analytical results discussing the detection of mechanical motion in the dispersive regime of the cavity and the qubit mode. We summarize and conclude our discussion in Sec. VI.

<sup>\*</sup>v.singh@iisc.ac.in

*Published by the American Physical Society under the terms of the Creative Commons Attribution 4.0 International license. Further distribution of this work must maintain attribution to the author(s) and the published article's title, journal citation, and DOI.*

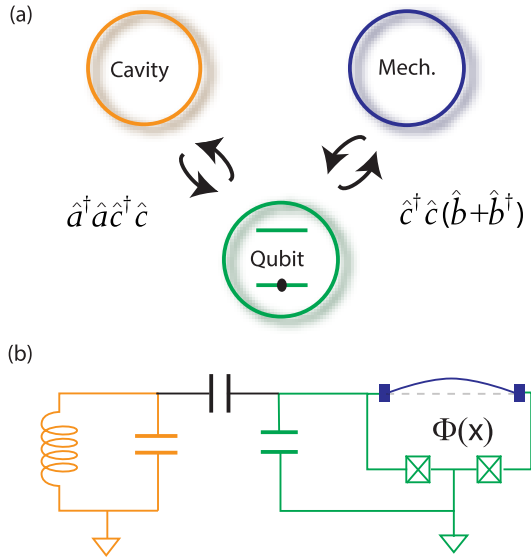


FIG. 1. (a) A conceptual schematic of the three-mode hybrid device showing a linear cavity coupled to a qubit which in turn couples to a mechanical resonator. A direct coupling between the cavity and the mechanical mode is not considered. (b) A possible implementation using a frequency tunable transmon qubit, where coupling to mechanical mode is achieved by embedding it in the SQUID loop and by applying a constant magnetic field. A magnetic field perpendicular (parallel) to the SQUID loop couples the in-plane (out-of-plane) mechanical mode to the qubit.

## II. THEORETICAL MODEL

We consider a coupled system where the mechanical mode modulates the transmon qubit frequency, therefore resulting in a longitudinal coupling. Such coupling between the transmon qubit and the mechanical resonator can be implemented by embedding a mechanical resonator into the superconducting quantum interference device (SQUID) loop of the qubit. In addition, the qubit couples to a linear mode (the readout cavity) transversely as in the circuit-QED setup. A schematic diagram of the system and a possible implementation with the equivalent circuit diagram are shown in the Figs. 1(a) and 1(b).

Using the dispersive approximation between the transmon and the readout cavity, we arrive at the following system Hamiltonian:

$$\hat{\mathcal{H}}_0 = \omega_c \hat{a}^\dagger \hat{a} + \omega_q \hat{c}^\dagger \hat{c} - \frac{\alpha_q}{2} \hat{c}^\dagger \hat{c}^\dagger \hat{c} \hat{c} + \omega_m \hat{b}^\dagger \hat{b} + \chi \hat{a}^\dagger \hat{a} \hat{c}^\dagger \hat{c} + g_0 \hat{c}^\dagger \hat{c} (\hat{b} + \hat{b}^\dagger), \quad (1)$$

where  $\hat{a}$  ( $\hat{a}^\dagger$ ),  $\hat{c}$  ( $\hat{c}^\dagger$ ), and  $\hat{b}$  ( $\hat{b}^\dagger$ ) are the annihilation (creation) operators for the cavity, qubit, and the mechanical mode of frequency  $\omega_c$ ,  $\omega_q$ , and  $\omega_m$ , respectively. The Kerr nonlinearity of the transmon is denoted as  $\alpha_q$ . The last two terms are the interaction terms between the modes. The dispersive coupling between the qubit and the readout cavity is denoted by  $\chi$ . The radiation-pressure type coupling between the transmon and the mechanical mode is denoted by the single-photon coupling rate  $g_0$ .

Two additional drive terms of amplitude  $\delta$  and  $\epsilon$  at frequency of  $\omega_L$  (near  $\omega_c$ ) and  $\omega_d$  (near  $\omega_q$ ) are added to the

Hamiltonian. The drive Hamiltonian can be written as

$$\hat{\mathcal{H}}_d = (\delta \hat{a} e^{+i\omega_L t} + \epsilon \hat{c} e^{+i\omega_d t}) + \text{H.c.} \quad (2)$$

By carrying out rotating frame transformations, given by the unitary operators  $U^a = \exp[i\omega_L \hat{a}^\dagger \hat{a} t]$  and  $U^c = \exp[i\omega_d \hat{c}^\dagger \hat{c} t]$ , the transformed Hamiltonian can be written as

$$\hat{\mathcal{H}} = -\Delta_c \hat{a}^\dagger \hat{a} - \Delta_q \hat{c}^\dagger \hat{c} - \frac{\alpha_q}{2} \hat{c}^\dagger \hat{c}^\dagger \hat{c} \hat{c} + \omega_m \hat{b}^\dagger \hat{b} + \chi \hat{a}^\dagger \hat{a} \hat{c}^\dagger \hat{c} + g_0 \hat{c}^\dagger \hat{c} (\hat{b} + \hat{b}^\dagger) + \delta (\hat{a} + \hat{a}^\dagger) + \epsilon (\hat{c} + \hat{c}^\dagger), \quad (3)$$

where  $\Delta_c = \omega_L - \omega_c$  and  $\Delta_q = \omega_d - \omega_q$ . In this frame of rotation, the transformed Hamiltonian becomes time independent. For further analysis, we shift to a mean-field frame using the following displacement transformation:

$$\mathcal{D}(\alpha, \mu, \beta) = \exp[\alpha(\hat{a} - \hat{a}^\dagger) + \mu(\hat{c} - \hat{c}^\dagger) + \beta(\hat{b} - \hat{b}^\dagger)], \quad (4)$$

where  $\alpha$ ,  $\mu$ , and  $\beta$  are real scalar quantities. For a particular choice of  $\alpha = \bar{\alpha}$ ,  $\mu = \bar{\mu}$ , and  $\beta = \bar{\beta}$ , all the drive terms (terms proportional to  $\hat{a} + \hat{a}^\dagger$ ,  $\hat{b} + \hat{b}^\dagger$ , and  $\hat{c} + \hat{c}^\dagger$ ) get canceled. After dropping the third- and higher-order terms, we arrive at the following effective Hamiltonian:

$$\hat{\mathcal{H}}' \approx -\tilde{\Delta}_c \hat{a}^\dagger \hat{a} - \tilde{\Delta}_q \hat{c}^\dagger \hat{c} - \eta(\hat{c}^2 + \hat{c}^{\dagger 2}) + \omega_m \hat{b}^\dagger \hat{b} + J(\hat{a} + \hat{a}^\dagger)(\hat{c} + \hat{c}^\dagger) + g(\hat{c} + \hat{c}^\dagger)(\hat{b} + \hat{b}^\dagger), \quad (5)$$

where  $\tilde{\Delta}_c = \Delta_c - \chi \bar{\mu}^2$ ,  $\tilde{\Delta}_q = \Delta_q + 2\alpha_q \bar{\mu}^2 - \chi \bar{\alpha}^2 - 2g_0 \bar{\beta}$ ,  $\eta = \frac{\alpha_q \bar{\mu}^2}{2}$ ,  $J = \chi \bar{\alpha} \bar{\mu}$ , and  $g = g_0 \bar{\mu}$ . It might be important to underline here that the coupling rates  $g$  and  $J$  as defined above are the scaled coupling rates. Both the coupling rates,  $g$  and  $J$ , show the scaling with drive tone amplitude similar to the case in a linear optomechanical device.

## III. EQUATIONS OF MOTION

Dynamics of the system depends on various decay rates associated with different modes and drive amplitudes. We write the equations of motion for the field operators while incorporating all the noise operators and decay rates as

$$\dot{\hat{a}} = -i[\hat{a}, \hat{\mathcal{H}}'] - \frac{\kappa}{2} \hat{a} + \sqrt{\kappa_{ex}} \hat{a}_{in} + \sqrt{\kappa_0} \hat{f}_{in}, \quad (6a)$$

$$\dot{\hat{c}} = -i[\hat{c}, \hat{\mathcal{H}}'] - \frac{\Gamma}{2} \hat{c} + \sqrt{\Gamma_{ex}} \hat{c}_{in} + \sqrt{\Gamma_0} \hat{\xi}_{in}, \quad (6b)$$

$$\dot{\hat{b}} = -i[\hat{b}, \hat{\mathcal{H}}'] - \frac{\gamma_m}{2} \hat{b} + \sqrt{\gamma_m} \hat{b}_{in}, \quad (6c)$$

where  $\hat{a}_{in}$ ,  $\hat{c}_{in}$ ,  $\hat{b}_{in}$ ,  $\hat{f}_{in}$ , and  $\hat{\xi}_{in}$  are the noise operators of cavity, qubit, and mechanical mode, respectively. The mechanical energy dissipation rate is  $\gamma_m$ . The internal, external, and total cavity (qubit) dissipation rates are  $\kappa_0$  ( $\Gamma_0$ ),  $\kappa_{ex}$  ( $\Gamma_{ex}$ ), and  $\kappa$  ( $\Gamma$ ), respectively. This set of equations can be solved by performing a Fourier transformation, defined as  $x[\omega] = \mathcal{F}[x(t)] = \int_{-\infty}^{+\infty} x(t) e^{i\omega t} dt$ , of the equations. We now define a field vector  $u[\omega] = [\hat{a}[\omega], (\hat{a}^\dagger)[\omega], \hat{c}[\omega], (\hat{c}^\dagger)[\omega], \hat{b}[\omega], (\hat{b}^\dagger)[\omega]]^T$  and evaluate its governing equation of the form

$$u[\omega] = (-i\omega \mathbb{1} - A)^{-1} r[\omega] = \mathcal{B} r[\omega], \quad (7)$$

where

$$r[\omega] = \begin{bmatrix} \sqrt{\kappa_{ex}} \hat{a}_{in}[\omega] + \sqrt{\kappa_0} \hat{f}_{in}[\omega] \\ \sqrt{\kappa_{ex}} (\hat{a}_{in}^\dagger)[\omega] + \sqrt{\kappa_0} (\hat{f}_{in}^\dagger)[\omega] \\ \sqrt{\Gamma_{ex}} \hat{c}_{in}[\omega] + \sqrt{\Gamma_0} \hat{\xi}_{in}[\omega] \\ \sqrt{\Gamma_{ex}} (\hat{c}_{in}^\dagger)[\omega] + \sqrt{\Gamma_0} (\hat{\xi}_{in}^\dagger)[\omega] \\ \sqrt{\gamma_m} \hat{b}_{in}[\omega] \\ \sqrt{\gamma_m} (\hat{b}_{in}^\dagger)[\omega] \end{bmatrix}. \quad (8)$$

The matrix  $\mathcal{B}$  can be calculated from Eqs. (5) and (6) as

$$\mathcal{B} = \begin{bmatrix} 1/\chi_c & 0 & iJ & iJ & 0 & 0 \\ 0 & 1/\tilde{\chi}_c & -iJ & -iJ & 0 & 0 \\ iJ & iJ & 1/\chi_q & -2i\eta & ig & ig \\ -iJ & -iJ & 2i\eta & 1/\tilde{\chi}_q & -ig & -ig \\ 0 & 0 & ig & ig & 1/\chi_m & 0 \\ 0 & 0 & -ig & -ig & 0 & 1/\tilde{\chi}_m \end{bmatrix}^{-1}. \quad (9)$$

All  $\chi$ 's in the matrix represent the susceptibility of the modes, defined as

$$\begin{aligned} \chi_c[\omega] &= \frac{1}{-i\omega - i\tilde{\Delta}_c + \frac{\kappa}{2}}; & \tilde{\chi}_c[\omega] &= \frac{1}{-i\omega + i\tilde{\Delta}_c + \frac{\kappa}{2}}, \\ \chi_q[\omega] &= \frac{1}{-i\omega - i\tilde{\Delta}_q + \frac{\Gamma}{2}}; & \tilde{\chi}_q[\omega] &= \frac{1}{-i\omega + i\tilde{\Delta}_q + \frac{\Gamma}{2}}, \\ \chi_m[\omega] &= \frac{1}{-i\omega + i\omega_m + \frac{\gamma_m}{2}}; & \tilde{\chi}_m[\omega] &= \frac{1}{-i\omega - i\omega_m + \frac{\gamma_m}{2}}. \end{aligned}$$

From Eq. (7), we can solve for the field operators. Further, we define the spectrum of any mode as

$$S_{\mathcal{O}}(\omega) = \frac{1}{2\pi} \int_{-\infty}^{+\infty} \langle (\hat{\mathcal{O}}[\omega'])^\dagger \hat{\mathcal{O}}[\omega] \rangle d\omega'. \quad (10)$$

Equation (10) and the solution of field operators can be used to get the spectrum of the modes. The detailed calculations and the correlators of noise operators are given in Appendix A. The calculated spectrum is as follows:

$$\begin{aligned} S_x(\omega)|_{x \in \{1,3,5\}} &= n_m^i \gamma_m (|\mathcal{B}_{x5}[\omega]|^2 + |\mathcal{B}_{x6}[\omega]|^2) \\ &+ \kappa |\mathcal{B}_{x2}[\omega]|^2 + \Gamma |\mathcal{B}_{x4}[\omega]|^2 + \gamma_m |\mathcal{B}_{x6}[\omega]|^2, \end{aligned} \quad (11)$$

where  $n_m^i$  is the initial phonon occupation in the mechanical mode. The indexing  $\{S_1, S_3, S_5\}$  maps to the spectrum of cavity, qubit, and mechanics as  $\{S_a, S_c, S_b\}$ , respectively.

#### IV. SPECTRUM OF THE QUBIT AND THE MECHANICAL MODE

In this section, we discuss the best cooling scenario of the mechanical resonator by inspecting the qubit and the mechanical spectrum. Figure 2 shows the spectrum of the transmon qubit for two different detunings of the drive tone  $\tilde{\Delta}_q = -1.0\omega_m$  (dashed blue line) and  $\tilde{\Delta}_q = -1.2\omega_m$  (solid orange line). In the presence of a nearly red-detuned drive on

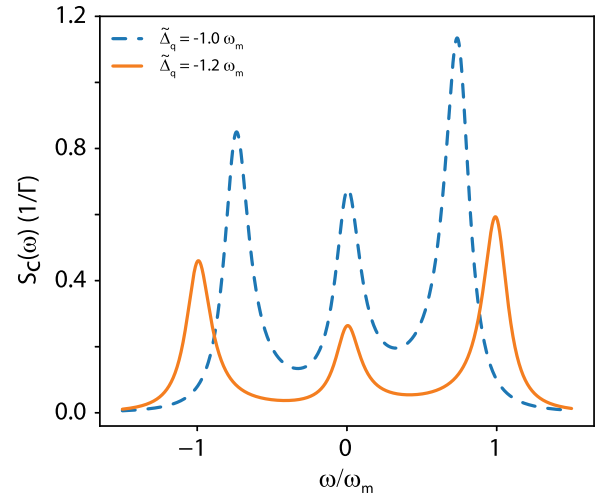


FIG. 2. Plot of the qubit spectrum for two different values of drive detunings,  $\tilde{\Delta}_q = -1.0\omega_m$  (dashed blue line) and  $\tilde{\Delta}_q = -1.2\omega_m$  (solid orange line). The parameters used for the plots are  $\tilde{\Delta}_c = 0$ ,  $\omega_m = 2\pi \times 6$  MHz,  $J = 2\pi \times 0.8$  MHz,  $g = 2\pi \times 2$  kHz,  $\kappa = 2\pi \times 4$  MHz,  $\omega_m/\Gamma = 5$ ,  $\gamma = 2\pi \times 6$  Hz, and  $\eta = 2\pi \times 2$  MHz.

qubit mode, its spectrum becomes asymmetric. The cooling rate is calculated from the asymmetry of the spectrum, which is large for a specific drive position. In the weak-coupling regime ( $g \ll \Gamma$ ), the cooling rate for the mechanical resonator is given by  $\Gamma_c = 2\{g^2[S_c(\omega_m) - S_c(-\omega_m)] + \gamma_m\}$  [12,17]. The optimum cooling rate, as seen from Fig. 2, is a function of the position of the drive [17]. Unlike a linear cavity as a bath for cooling, the cooling rate of a mechanical resonator for an anharmonic oscillator (the qubit) depends on the position of the cooling tone applied and the anharmonicity of the resonator mode. This is a direct consequence of the Kerr term. In the steady state, the final phonon occupancy can be calculated from the cooling rate and the qubit spectrum as

$$n_f = 2 \frac{n_m^i \gamma_m}{\Gamma_c} + 2g^2 \frac{S_c(-\omega_m)}{\Gamma_c}. \quad (12)$$

To further understand the backaction on the mechanical resonator due to a drive on the qubit mode, we compute the mechanical spectrum  $S_b(\omega)$ . In the steady state, the mean phonon occupancy of the mechanical mode can be calculated as  $n_f = \frac{1}{2\pi} \int S_b(\omega) d\omega$ , which is the area under the Lorentzian in the mechanical mode spectrum. While it is possible to reduce the expression of the mechanical spectrum to a Lorentzian form, we find it more efficient to compute the spectrum and carry out a numerical fit to extract the effective linewidth and the effective resonant frequency. Figures 3(a) and 3(b) show the linewidth broadening and resonant frequency shift of the mechanical mode, for a red-detuned ( $\tilde{\Delta}_q = -1.2\omega_m$ ) qubit drive. The backaction on the mechanical resonator from the drive on qubit is reflected in the change of mechanical frequency and an increase in the effective linewidth. The final phonon occupancy is plotted in Fig. 3(c) for different values of sideband parameter  $\omega_m/\Gamma$ . It is evident from the figure that in the steady driving of the qubit, the final phonon occupancy strongly depends on sideband parameter  $\omega_m/\Gamma$ .

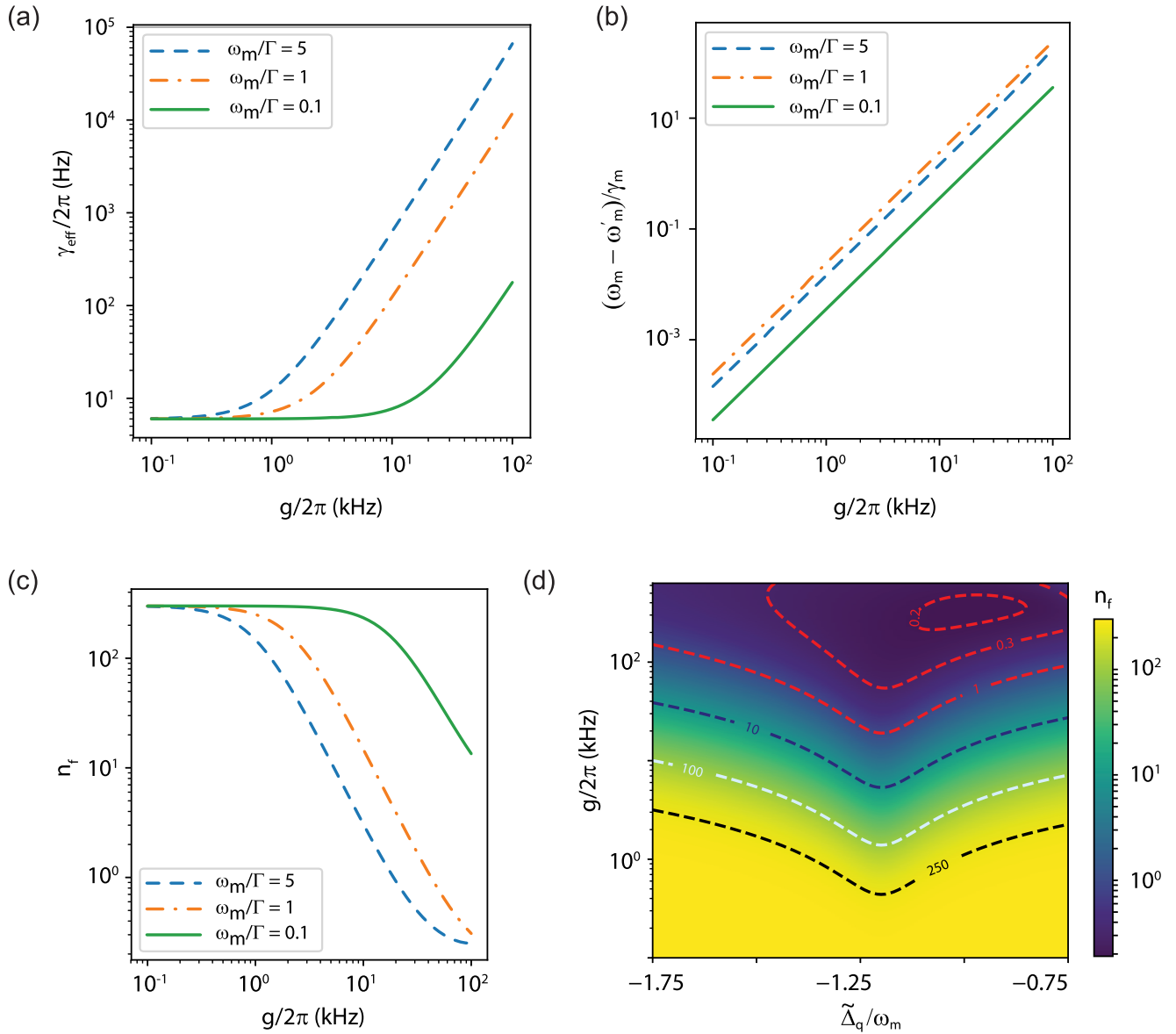


FIG. 3. Cooling of the mechanical mode: The spectrum of the mechanical mode is analyzed to characterize the effect of backaction arising from the drive tone near the qubit frequency  $\omega_q$ . The extracted parameters for effective mechanical linewidth and shift in the mechanical resonant frequency as the electromechanical coupling between the qubit and the mechanical mode is varied, are shown in (a) and (b). Panel (c) shows the final phonon occupancy ( $n_f$ ) of the mechanical mode. It is extracted by calculating the area under the Lorentzian in the mechanical spectrum. For large qubit-mechanics coupling a final phonon occupation well below 1 can be achieved for various sideband parameters. The dashed, dot-dashed, and solid lines correspond to  $\omega_m/\Gamma = 5$ ,  $\omega_m/\Gamma = 1$ , and  $\omega_m/\Gamma = 0.1$ , respectively. (d) Final phonon occupancy as a function of qubit-mechanics coupling and scaled detuning between the drive and the qubit frequency for  $\omega_m/\Gamma = 5$ . The parameters used for the plots are  $\tilde{\Delta}_c = 0$ ,  $\omega_m = 2\pi \times 6$  MHz,  $J = 2\pi \times 0.8$  MHz,  $\eta = 2\pi \times 2$  MHz,  $\kappa = 2\pi \times 4$  MHz,  $\gamma = 2\pi \times 6$  Hz, and  $n_m^i = 300$ . For the plot in panels (a), (b), and (c), we use  $\tilde{\Delta}_q = -1.2\omega_m$  as the detuning.

A larger value of sideband parameter offers better cooling of the mechanical mode. It is important to underline here that the cooling to the quantum ground state of the mechanical resonator is possible well before entering the strong-coupling regime,  $g \gtrsim \max(\Gamma, \kappa)$ .

To gain insight into the spectrum calculation, we consider a simpler case when qubit anharmonicity is set to zero,  $\eta = 0$ , and it is being driven at the lower mechanical sideband  $\tilde{\Delta}_q = -\omega_m$ . With these parameters and Eq. (10), the mechanical

spectrum can be approximately written as

$$S_b(\omega) = \frac{n_m^i \gamma_m \Gamma^2 / (\Gamma^2 - 8g^2)}{(\omega - \omega_m)^2 + \frac{(4g^2 + \gamma_m \Gamma)^2}{4(\Gamma^2 - 8g^2)}}. \quad (13)$$

From this simplified expression of the mechanical spectrum, we can write the effective linewidth of the mechanical resonator as  $\gamma_{\text{eff}} = \frac{4g^2 + \gamma_m \Gamma}{\sqrt{\Gamma^2 - 8g^2}} \simeq \gamma_m(C + 1)$ , where  $C = \frac{4g^2}{\gamma_m \Gamma}$  is

defined as the cooperativity. Similarly, the final mean phonon occupation can be written as  $n_f = \frac{n_m^i \gamma_m \Gamma^2}{4g^2 + \gamma_m \Gamma} \frac{1}{\sqrt{\Gamma^2 - 8g^2}} \approx \frac{n_m^i}{1+C}$  for  $\Gamma \gg g$ . We note that in the limit of zero anharmonicity and weak coupling, the results are consistent with that obtained from linear cavity optomechanics [2].

For the model Hamiltonian given by Eq. (5), the mean phonon occupation can also be obtained by solving the Lindblad master equation. Here, we obtain the equations of motion for the expectation values of mode operators and solve for the steady-state solutions. From this formalism, we calculate the steady-state occupancy in the mechanical mode for the various drive detuning  $\tilde{\Delta}_q$  and coupling  $g$ . Figure 3(d) shows the color plot of the final phonon occupation for the sideband parameter of  $\omega_m/\Gamma = 5$ . We can see that the optimum cooling can be achieved near the detuning of  $\tilde{\Delta}_q \approx -1.2\omega_m$ . It is important to emphasize here that the lowest phonon occupation of the mechanical resonator depends on the device parameters, such as qubit thermal occupation and dissipation rate  $\Gamma$ . For the calculations presented in this section, we assumed the thermal occupation of the qubit and readout cavity to be zero. Another important parameter that affects the ultimate performance of the sideband cooling is sideband parameter  $\omega_m/\Gamma$  [12], and cooling to the ground state can only be achieved in the sideband-resolved limit  $\omega_m/\Gamma \gtrsim 1$ .

## V. EXPERIMENTAL DETAILS

After discussing the performance of the sideband cooling when the qubit is dispersively coupled to the readout cavity, we address the next question on the possibility of the mechanical readout. In the dispersive regime, there is no direct coupling between the cavity and the mechanical resonator. The modulation of qubit frequency translates to the cavity mode via dispersive coupling, thus creating an effective coupling between the cavity and the mechanical motion. By tuning the transmon qubit frequency near half flux quantum, a large electromechanical coupling with the qubit mode can be obtained. However, when  $|\omega_q - \omega_c|$  is large, the effective coupling between the cavity and mechanical mode is suppressed. Next, we show that the addition of cooling tone near the qubit frequency is helpful for the readout of the mechanical motion.

For experimental realization, we use a device consisting of a transmon qubit with a doubly clamped suspended nanowire embedded in the SQUID loop. For the qubit readout, we use a three-dimensional copper rectangular waveguide cavity. The scanning electron microscope (SEM) image of the device is shown in Fig. 4(a). The transmon, fabricated on a silicon substrate coated with highly stressed SiN, is designed to have tunable frequency realized via SQUID. One arm of the SQUID is made suspended to form a nanowire, essentially establishing the mechanical mode. The silicon substrate is placed inside the readout cavity and cooled down to 20 mK in a dilution refrigerator. A detailed description of the device fabrication methods and the measurement setup can be found in Ref. [31].

Figure 4(b) shows the cavity transmission amplitude  $|S_{21}|$  as the magnetic flux through the SQUID loop is varied. When the qubit is brought in resonance with the cavity mode, the vacuum-Rabi splitting is observed and two hybrid modes emerge as indicated by the dashed box in Fig. 4(b). From

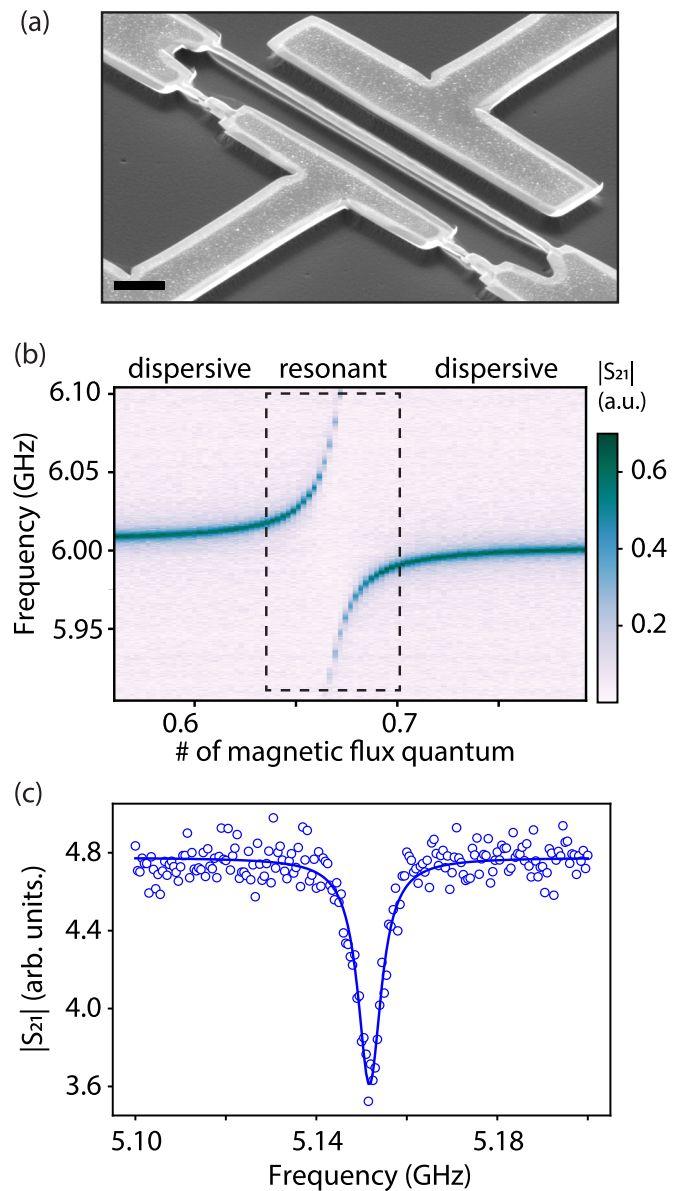


FIG. 4. (a) A SEM image of the device showing the suspended part of the SQUID loop and the Josephson junctions. The length and width of the nanowire is  $40 \mu\text{m}$  and  $200 \text{nm}$ , respectively. The scale bar corresponds to  $5 \mu\text{m}$ . (b) Color plot of the cavity transmission  $|S_{21}|$  as a function of the magnetic flux through the SQUID loop. (c) Two-tone measurements spectroscopic linewidth of the qubit in the dispersive regime.

the avoided crossing, we determine the qubit-cavity coupling strength to be 75 MHz. We measure the dressed cavity frequency to be 6.006 GHz, the maximum qubit frequency to be 7.8 GHz, and the qubit anharmonicity to be  $-130 \text{MHz}$ . We apply a magnetic field of  $B \approx 1.1 \text{mT}$ , perpendicular to the plane of the SQUID loop. It couples the in-plane motion of the mechanical resonator to the qubit.

To operate in the dispersive limit, we choose a qubit detuning  $\Delta = \omega_q - \omega_c$  of  $-2\pi \times 900 \text{MHz}$ . A representative two-tone measurement of the qubit is shown in Fig. 4(c). To record the mechanical motion at this operating point, we apply two tones to the device, a drive tone near the qubit frequency

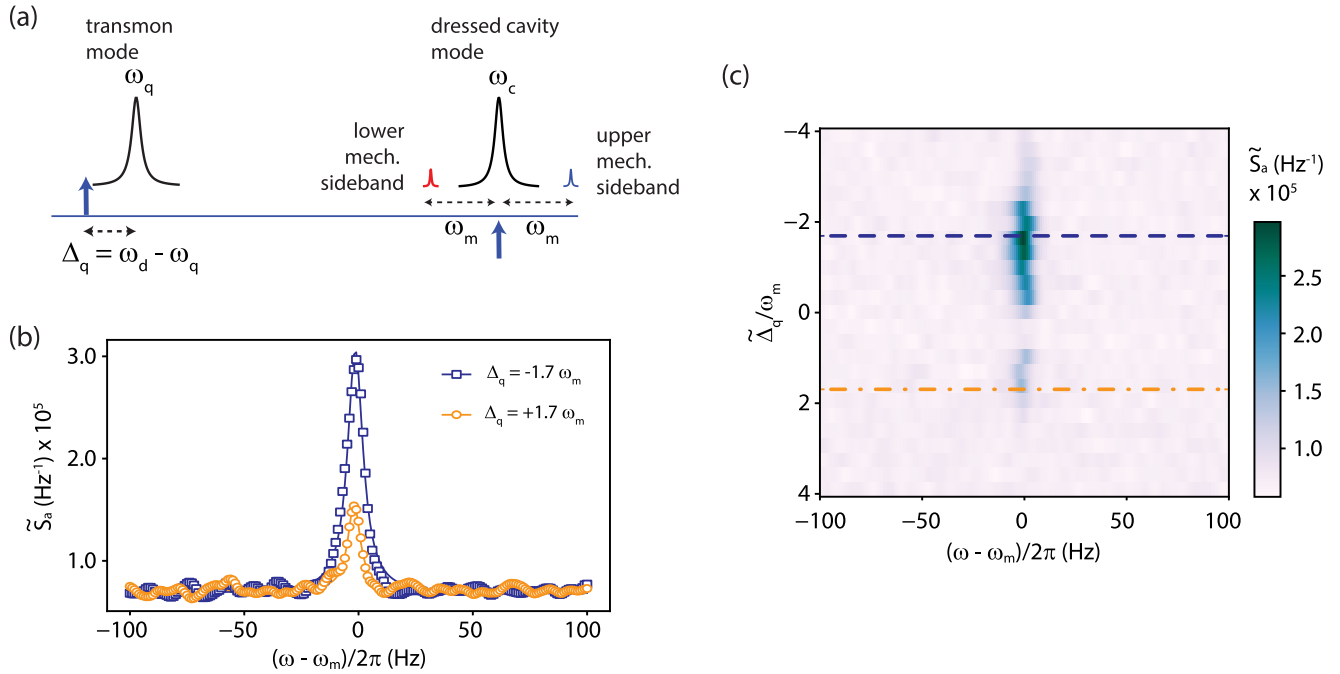


FIG. 5. Experimental data: power spectral density of the cavity mode is measured while varying the drive detuning from the qubit mode. (a) Schematic of the measurement process showing a drive tone present near the qubit mode. The detuning between the qubit and the drive frequency is changed during the measurement. A probe of frequency  $\omega_c$  is added and its lower and upper mechanical sidebands are recorded with a spectrum analyzer. (b) The spectral density is shown for the drive detuning of  $\tilde{\Delta}_q = -1.7\omega_m$  (blue square) and  $\tilde{\Delta}_q = +1.7\omega_m$  (orange circle). The difference in the magnitude of the spectrum as the detuning changes sign is evident. The mechanical resonator has a frequency of  $\omega_m/2\pi \approx 5.9$  MHz and a linewidth  $\gamma_m/2\pi = 6$  Hz. (c) A color plot of normalized spectral density as a function of detuning and measurement frequency.

and a probe tone near  $\omega_c$ , and record the mechanical sidebands of the probe tone using a spectrum analyzer. The positioning of various frequencies and drive tones is shown in Fig. 5(a).

Figure 5(b) shows the recorded spectrum for two different detunings. The experimentally measured microwave spectrum  $S_{mw}(\omega)$  is normalized and represented in the units of intracavity photons defined as  $\tilde{S}_a = S_{mw}(\omega)/(\hbar\omega_c G\kappa_{ex} \text{RBW})$ , where  $G$  is the estimated net gain of the output line,  $\kappa_{ex}$  is the external coupling rate of the output port of the cavity, and RBW is the resolution bandwidth of the spectrum analyzer. Clearly, the spectrum has a larger peak for negative detuning (blue square) as compared to that for the positive detuning (orange circle). This asymmetry becomes quite evident as the detuning of the qubit drive is varied. Figure 5(c) shows the color plot of  $\tilde{S}_a$  as the drive frequency is varied across the qubit transition.

The mechanical resonator has a frequency of  $\omega_m/2\pi \approx 5.9$  MHz and a linewidth of  $\gamma_m/2\pi \approx 6$  Hz. Here, we do not observe any backaction on the mechanical resonator. Both, the mechanical frequency and the linewidth do not show any measurable change as the detuning  $\tilde{\Delta}_q$  is varied across the qubit frequency. This is expected behavior within the experimental parameters. For these measurements, we estimated a single-photon coupling rate of  $g_0/2\pi \approx 7.5$  kHz, and measured a qubit linewidth of  $\Gamma/2\pi \approx 15$  MHz. The lower sideband parameter and single-photon coupling rate reduces the effect of backaction from the qubit drive.

Another aspect of the measurement is the enhancement of the transduction and asymmetry with respect to  $\tilde{\Delta}_q$ . Qualitatively, it can be understood from the qubit-cavity dispersive

coupling and the Kerr term of the qubit mode. A drive tone near the qubit frequency acts like a parametric pump due to the qubit nonlinearity, resulting in the amplification of the field fluctuations due to electromechanical coupling. Further, due to the dispersive interaction between the qubit and the cavity mode, these field fluctuations result in the modulation of the intracavity probe field, and hence in an improved transduction. The asymmetry in the response is a direct manifestation of the weak anharmonicity of the qubit.

To quantitatively understand the enhancement in the transduction and the asymmetry in spectral density with respect to  $\tilde{\Delta}_q$ , we compute the cavity spectrum from Eq. (10) as a function of susceptibilities. Approximately, the cavity spectral density can be written as

$$S_a(\omega) \approx n_m^i \gamma_m (|\chi_m|^2 + |\tilde{\chi}_m|^2) \sigma(\omega), \quad \text{where} \quad (14)$$

$$\sigma(\omega) = \left| \frac{gJ\chi_c\chi_{q\bar{q}}(\Delta_q - 2\eta)}{\Delta_q + 2i\eta^2\chi_{q\bar{q}} + g^2\chi_{m\bar{m}}\chi_{q\bar{q}}(\Delta_q - 2\eta)} \right|^2, \quad (15)$$

$$\chi_{q\bar{q}} = \chi_q - \tilde{\chi}_q, \quad (16)$$

$$\chi_{m\bar{m}} = \chi_m - \tilde{\chi}_m. \quad (17)$$

Here, we note that the presence of the effective anharmonicity  $\eta$  in the above equation accounts for the asymmetry observed with respect to the detuning of qubit drive. In the limit  $\eta \rightarrow 0$ , the expression of  $\sigma$  becomes symmetric with respect to  $\Delta_q$  as it enters the expression through  $\chi_{q\bar{q}}$  only.

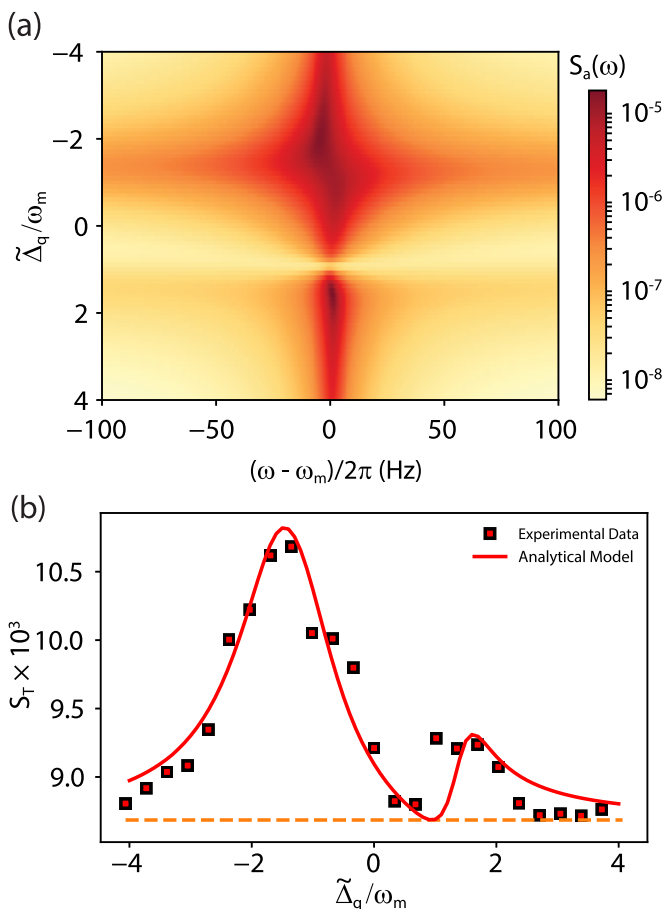


FIG. 6. (a) Plot of the calculated cavity mode spectrum from the theoretical model as a function of detuning  $\tilde{\Delta}_q$  and frequency. Parameters are taken from the device studied here, as described in the main text. (b) Plot of integrated spectrum  $S_T = \int S_a(\omega)d\omega$  for different detuning is calculated from the theoretical and experimental results. The square points indicate the experimental data, plotted as a function of drive detuning ( $\tilde{\Delta}_q$ ). The solid curve is plotted using the estimated device parameters and the analytical expression. The dashed straight line indicates the noise level of the measurements. The parameters used for the plots:  $\tilde{\Delta}_c = 0$ ,  $\omega_m = 2\pi \times 5.9$  MHz,  $J = 2\pi \times 5.6$  MHz,  $g = 2\pi \times 3.6$  kHz,  $\eta = 2\pi \times 2.8$  MHz,  $\kappa = 2\pi \times 4$  MHz,  $\Gamma = 2\pi \times 8$  MHz,  $\gamma_m = 2\pi \times 6$  Hz, and  $n_m^i = 350$ .

Similar to the measurement performed, we analyze the cavity spectral density as  $\tilde{\Delta}_q$  is varied. Figure 6(a) shows theoretically calculated  $\tilde{S}_a(\omega)$  using the device parameters. We observe a pattern in  $S_a(\omega)$  which is similar to the experimental measurement. For a quantitative comparison, we define the integrated spectrum as  $S_T = \int S_a(\omega)d\omega$  and evaluate it for experimental data. Figure 6(b) shows the plot of  $S_T$  from the experimental results shown in Fig. 5(c) and theoretical calculations. A good match validates the approximation made in arriving at the effective Hamiltonian in the theoretical calculations.

## VI. OUTLOOK AND CONCLUSION

To summarize, this work has investigated a coupled three-mode hybrid system with a transmon qubit in the presence

of external drives. Using the quantum noise and the Lindblad formalism, we study the possibility of sideband cooling of the mechanical resonator by the qubit mode. We find that the readout of the mechanical resonator is possible by coupling the transmon qubit to a readout cavity just like in standard c-QED setup while maintaining a dispersive coupling between the cavity and the qubit. In addition, we experimentally demonstrate the applicability of the readout scheme, wherein the experimental results match closely to the analytical calculations. In this particular experiment, we do not observe any cooling of the mechanical resonator due to lower  $g_0$  and low sideband parameter ( $\omega_m/\Gamma \approx 0.4$ ). While the achieved flux responsivity of the qubit in dispersive limit was high,  $16 \text{ GHz}/\Phi_0$ , the estimated coupling rate ( $g_0/2\pi \approx 7.5 \text{ kHz}$ ) was inadequate due to the lower applied magnetic field, 1.1 mT.

Looking ahead, the recent experiments have shown promising results for the transmon linewidth in the parallel magnetic field up to hundreds of millitesla with no significant change in the spectroscopic linewidth [42]. In addition, the flux responsivity of the qubit can be pushed to  $40 \text{ GHz}/\Phi_0$  by increasing the maximum qubit frequency. With these parameters, the single-photon electromechanical coupling between the qubit and mechanical resonator can be enhanced up to 10 MHz, bringing the system near to ultrastrong-coupling regime [43]. Such regime opens up the possibilities of observing the photon blockade effects [10], nontrivial ground state [7], and a path of using a low-frequency mechanical resonator in the quantum technologies.

## ACKNOWLEDGMENTS

The authors thank G. S. Agarwal and Manas Kulkarni for valuable discussions. This material is based upon work supported by the Air Force Office of Scientific Research under Award No. FA2386-20-1-4003. V.S. acknowledges the support received under the Core Research Grant by the Department of Science and Technology (India). The authors acknowledge device fabrication facilities at CeNSE, IISc Bangalore, and central facilities at the Department of Physics funded by DST.

## APPENDIX A: CALCULATIONS OF THE CAVITY MODE SPECTRUM

Spectrum of the cavity mode is calculated from Eq. (10) in the main text. In the cavity operator, it can be written as

$$S_a(\omega) = \frac{1}{2\pi} \int_{-\infty}^{+\infty} \langle (\hat{a}[\omega'])^\dagger \hat{a}[\omega] \rangle d\omega'. \quad (\text{A1})$$

Equation (7) is used to calculate the steady-state value of  $\hat{a}[\omega]$ , which can be written as

$$\hat{a}[\omega] = (\mathcal{B} r[\omega])_{11} = \sum_j \mathcal{B}_{1j}(r[\omega])_{j1}, \quad (\text{A2})$$

where  $r[\omega]$  is a column matrix of noise operators of all the modes.

$$r[\omega] = \begin{bmatrix} \sqrt{\kappa_{ex}} \hat{a}_{in}[\omega] + \sqrt{\kappa_0} \hat{f}_{in}[\omega] \\ \sqrt{\kappa_{ex}} (\hat{a}_{in}^\dagger)[\omega] + \sqrt{\kappa_0} (\hat{f}_{in}^\dagger)[\omega] \\ \sqrt{\Gamma_{ex}} \hat{c}_{in}[\omega] + \sqrt{\Gamma_0} \hat{\xi}_{in}[\omega] \\ \sqrt{\Gamma_{ex}} (\hat{c}_{in}^\dagger)[\omega] + \sqrt{\Gamma_0} (\hat{\xi}_{in}^\dagger)[\omega] \\ \sqrt{\gamma_m} \hat{b}_{in}[\omega] \\ \sqrt{\gamma_m} (\hat{b}_{in}^\dagger)[\omega] \end{bmatrix}. \quad (\text{A3})$$

The noise operators in the frequency domain satisfy the following relations:

$$\langle \hat{a}_{in}[\omega] (\hat{a}_{in}[\omega'])^\dagger \rangle = 2\pi \delta(\omega - \omega'); \quad \langle (\hat{a}_{in}[\omega])^\dagger \hat{a}_{in}[\omega'] \rangle = 0, \quad (\text{A4a})$$

$$\langle \hat{f}_{in}[\omega] (\hat{f}_{in}[\omega'])^\dagger \rangle = 2\pi \delta(\omega - \omega'); \quad \langle (\hat{f}_{in}[\omega])^\dagger \hat{f}_{in}[\omega'] \rangle = 0, \quad (\text{A4b})$$

$$\langle \hat{c}_{in}[\omega] (\hat{c}_{in}[\omega'])^\dagger \rangle = 2\pi \delta(\omega - \omega'); \quad \langle (\hat{c}_{in}[\omega])^\dagger \hat{c}_{in}[\omega'] \rangle = 0, \quad (\text{A4c})$$

$$\langle \hat{\xi}_{in}[\omega] (\hat{\xi}_{in}[\omega'])^\dagger \rangle = 2\pi \delta(\omega - \omega'); \quad \langle (\hat{\xi}_{in}[\omega])^\dagger \hat{\xi}_{in}[\omega'] \rangle = 0, \quad (\text{A4d})$$

$$\langle \hat{b}_{in}[\omega] (\hat{b}_{in}[\omega'])^\dagger \rangle = 2\pi (n_m^i + 1) \delta(\omega - \omega'), \quad (\text{A4e})$$

$$\langle (\hat{b}_{in}[\omega])^\dagger \hat{b}_{in}[\omega'] \rangle = 2\pi n_m^i \delta(\omega - \omega'), \quad (\text{A4f})$$

where  $n_m^i$  is the thermal phonon occupancy of the mechanical mode. We can expand Eq. (A2) and write the solution of  $\hat{a}[\omega]$  as

$$\begin{aligned} \hat{a}[\omega] = & \sqrt{\kappa_{ex}} \mathcal{B}_{11}[\omega] \hat{a}_{in}[\omega] + \sqrt{\kappa_0} \mathcal{B}_{11}[\omega] \hat{f}_{in}[\omega] + \sqrt{\kappa_{ex}} \mathcal{B}_{12}[\omega] (\hat{a}_{in}^\dagger)[\omega] + \sqrt{\kappa_0} \mathcal{B}_{12}[\omega] (\hat{f}_{in}^\dagger)[\omega] + \sqrt{\Gamma_{ex}} \mathcal{B}_{13}[\omega] \hat{c}_{in}[\omega] \\ & + \sqrt{\Gamma_0} \mathcal{B}_{13}[\omega] \hat{\xi}_{in}[\omega] + \sqrt{\Gamma_{ex}} \mathcal{B}_{14}[\omega] (\hat{c}_{in}^\dagger)[\omega] + \sqrt{\Gamma_0} \mathcal{B}_{14}[\omega] (\hat{\xi}_{in}^\dagger)[\omega] + \sqrt{\gamma_m} \mathcal{B}_{15}[\omega] \hat{b}_{in}[\omega] + \sqrt{\gamma_m} \mathcal{B}_{16}[\omega] (\hat{b}_{in}^\dagger)[\omega]. \end{aligned} \quad (\text{A5})$$

By using the identity  $(x^\dagger)[\omega] = (x[-\omega])^\dagger$ , we can rewrite the solution of  $\hat{a}[\omega]$ .

$$\begin{aligned} \hat{a}[\omega] = & \sqrt{\kappa_{ex}} \mathcal{B}_{11}[\omega] \hat{a}_{in}[\omega] + \sqrt{\kappa_0} \mathcal{B}_{11}[\omega] \hat{f}_{in}[\omega] + \sqrt{\kappa_{ex}} \mathcal{B}_{12}[\omega] (\hat{a}_{in}[-\omega])^\dagger + \sqrt{\kappa_0} \mathcal{B}_{12}[\omega] (\hat{f}_{in}[-\omega])^\dagger + \sqrt{\Gamma_{ex}} \mathcal{B}_{13}[\omega] \hat{c}_{in}[\omega] \\ & + \sqrt{\Gamma_0} \mathcal{B}_{13}[\omega] \hat{\xi}_{in}[\omega] + \sqrt{\Gamma_{ex}} \mathcal{B}_{14}[\omega] (\hat{c}_{in}[-\omega])^\dagger + \sqrt{\Gamma_0} \mathcal{B}_{14}[\omega] (\hat{\xi}_{in}[-\omega])^\dagger + \sqrt{\gamma_m} \mathcal{B}_{15}[\omega] \hat{b}_{in}[\omega] + \sqrt{\gamma_m} \mathcal{B}_{16}[\omega] (\hat{b}_{in}[-\omega])^\dagger. \end{aligned} \quad (\text{A6})$$

From the above equation and Eq. (A4), we can calculate  $\langle (\hat{a}[\omega'])^\dagger \hat{a}[\omega] \rangle$ ,

$$\begin{aligned} \langle (\hat{a}[\omega'])^\dagger \hat{a}[\omega] \rangle = & 2\pi \kappa_{ex} \mathcal{B}_{12}^*[\omega'] \mathcal{B}_{12}[\omega] \delta(\omega - \omega') + 2\pi \kappa_0 \mathcal{B}_{12}^*[\omega'] \mathcal{B}_{12}[\omega] \delta(\omega - \omega') + 2\pi \Gamma_{ex} \mathcal{B}_{14}^*[\omega'] \mathcal{B}_{14}[\omega] \delta(\omega - \omega') \\ & + 2\pi \Gamma_0 \mathcal{B}_{14}^*[\omega'] \mathcal{B}_{14}[\omega] \delta(\omega - \omega') + 2\pi n_m^i \gamma_m \mathcal{B}_{15}^*[\omega'] \mathcal{B}_{15}[\omega] \delta(\omega' - \omega) + 2\pi (n_m^i + 1) \gamma_m \mathcal{B}_{16}^*[\omega'] \mathcal{B}_{16}[\omega] \delta(\omega - \omega'). \end{aligned} \quad (\text{A7})$$

Substituting this to Eq. (10), the spectrum of the cavity mode can be written as

$$S_a(\omega) = n_m^i \gamma_m (|\mathcal{B}_{15}[\omega]|^2 + |\mathcal{B}_{16}[\omega]|^2) + \kappa |\mathcal{B}_{12}[\omega]|^2 + \Gamma |\mathcal{B}_{14}[\omega]|^2 + \gamma_m |\mathcal{B}_{16}[\omega]|^2, \quad (\text{A8})$$

where  $\kappa$ ,  $\Gamma$ , and  $\gamma_m$  are total dissipation rates of the cavity, qubit, and mechanical mode, respectively.  $n_m^i$  is the initial mechanical mode occupancy. The terms  $\mathcal{B}_{12}[\omega]$ ,  $\mathcal{B}_{14}[\omega]$ ,  $\mathcal{B}_{15}[\omega]$ , and  $\mathcal{B}_{16}[\omega]$  are calculated using Wolfram *Mathematica*.

$$\mathcal{B}_{12}[\omega] = -\frac{J^2 \chi_c \tilde{\chi}_c [-i\tilde{\chi}_q + \chi_q(i + 4\eta\tilde{\chi}_q)]}{-4i\eta^2 \chi_q \tilde{\chi}_q + J^2(\chi_c - \tilde{\chi}_c)[-i\tilde{\chi}_q + \chi_q(i + 4\eta\tilde{\chi}_q)] + i[1 + g^2(\chi_q - \tilde{\chi}_q)(\chi_m - \tilde{\chi}_m)] + 4g^2\eta\chi_q\tilde{\chi}_q(\chi_m - \tilde{\chi}_m)}, \quad (\text{A9a})$$

$$\mathcal{B}_{14}[\omega] = \frac{J\chi_c(1 + 2i\eta\chi_q)\tilde{\chi}_q}{-4i\eta^2 \chi_q \tilde{\chi}_q + J^2(\chi_c - \tilde{\chi}_c)[-i\tilde{\chi}_q + \chi_q(i + 4\eta\tilde{\chi}_q)] + i[1 + g^2(\chi_q - \tilde{\chi}_q)(\chi_m - \tilde{\chi}_m)] + 4g^2\eta\chi_q\tilde{\chi}_q(\chi_m - \tilde{\chi}_m)}, \quad (\text{A9b})$$

$$\mathcal{B}_{15}[\omega] = -\frac{gJ\chi_c[-i\tilde{\chi}_q + \chi_q(i + 4\eta\tilde{\chi}_q)]\chi_m}{-4i\eta^2 \chi_q \tilde{\chi}_q + J^2(\chi_c - \tilde{\chi}_c)[-i\tilde{\chi}_q + \chi_q(i + 4\eta\tilde{\chi}_q)] + i[1 + g^2(\chi_q - \tilde{\chi}_q)(\chi_m - \tilde{\chi}_m)] + 4g^2\eta\chi_q\tilde{\chi}_q(\chi_m - \tilde{\chi}_m)}, \quad (\text{A9c})$$

$$\mathcal{B}_{16}[\omega] = -\frac{gJ\chi_c[-i\tilde{\chi}_q + \chi_q(i + 4\eta\tilde{\chi}_q)]\tilde{\chi}_m}{-4i\eta^2 \chi_q \tilde{\chi}_q + J^2(\chi_c - \tilde{\chi}_c)[-i\tilde{\chi}_q + \chi_q(i + 4\eta\tilde{\chi}_q)] + i[1 + g^2(\chi_q - \tilde{\chi}_q)(\chi_m - \tilde{\chi}_m)] + 4g^2\eta\chi_q\tilde{\chi}_q(\chi_m - \tilde{\chi}_m)}. \quad (\text{A9d})$$

## APPENDIX B: CALCULATION OF THE FINAL MECHANICAL OCCUPATION USING THE LINDBLAD FORMALISM

From the Lindblad formalism the time-domain master equation of the density operator  $\hat{\rho}(t)$  is written as

$$\begin{aligned} \dot{\hat{\rho}} = & i[\hat{\rho}, \tilde{\mathcal{H}}] + \kappa(n_c^i + 1)\mathcal{D}[\hat{a}]\hat{\rho} + \kappa n_c^i \mathcal{D}[\hat{a}^\dagger]\hat{\rho} + \Gamma(n_q^i + 1)\mathcal{D}[\hat{c}]\hat{\rho} + \Gamma n_q^i \mathcal{D}[\hat{c}^\dagger]\hat{\rho} + \frac{\Gamma_\phi}{2}\mathcal{D}[\hat{c}^\dagger\hat{c}]\hat{\rho} \\ & + \gamma_m(n_m^i + 1)\mathcal{D}[\hat{b}]\hat{\rho} + \gamma_m n_m^i \mathcal{D}[\hat{b}^\dagger]\hat{\rho}. \end{aligned} \quad (\text{B1})$$

Here  $\kappa$  and  $\gamma_m$  are the energy relaxation rates of the cavity and mechanical mode. Qubit relaxation and pure dephasing are represented as  $\Gamma$  and  $\Gamma_\phi$ . The initial thermal occupancy of the cavity, qubit, and the mechanical modes are  $n_c^i$ ,  $n_q^i$ , and  $n_m^i$ , respectively. For our calculation we have considered  $\Gamma_\phi = 0$ .  $\mathcal{D}[\hat{O}]$  is the Lindblad superoperator written as

$$\mathcal{D}[\hat{O}]\rho := \hat{O}\rho\hat{O}^\dagger - \frac{1}{2}\hat{O}^\dagger\hat{O}\rho - \frac{1}{2}\rho\hat{O}^\dagger\hat{O}. \tag{B2}$$

We write down the equation of motion from the Hamiltonian in Eq. (5). This is to calculate the expectation values of different operators. The coupled linear equations are written in the matrix form,

$$\dot{\mathbf{d}} = \mathcal{M}\mathbf{d} + \mathcal{N}, \tag{B3}$$

where  $\mathbf{d}$  is the column matrix consisting of the expectation values of

$$\hat{a}^\dagger\hat{a}, \hat{b}^\dagger\hat{b}, \hat{c}^\dagger\hat{c}, \hat{a}^2, \hat{a}^{\dagger 2}, \hat{b}^2, \hat{b}^{\dagger 2}, \hat{c}^2, \hat{c}^{\dagger 2}, \hat{a}\hat{b}, \hat{a}^\dagger\hat{b}^\dagger, \hat{a}^\dagger\hat{b}, \hat{a}\hat{b}^\dagger, \hat{c}\hat{b}, \hat{c}^\dagger\hat{b}^\dagger, \hat{c}^\dagger\hat{b}, \hat{c}\hat{b}^\dagger, \hat{a}\hat{c}, \hat{a}^\dagger\hat{c}^\dagger, \hat{a}^\dagger\hat{c}, \hat{a}\hat{c}^\dagger. \tag{B4}$$

$$\mathcal{M} = \begin{bmatrix} 0 & 0 & -4i\eta & 0 & 0 & 0 & 0 & 0 & 0 & 1/\chi_{\hat{c}\hat{c}}^* & 0 & 0 & 0 & 0 & 2ig & 2ig & 0 & 0 & 2iJ & 0 & 2iJ \\ 0 & 0 & 0 & 0 & 0 & 0 & 0 & 0 & 0 & 0 & 1/\chi_{\hat{a}\hat{b}}^* & 0 & 0 & 0 & -iJ & 0 & -iJ & 0 & -ig & 0 & -ig \\ 0 & 0 & 0 & 0 & 0 & 0 & 0 & 0 & 0 & 0 & 0 & 1/\chi_{\hat{a}\hat{b}}^* & 0 & 0 & 0 & iJ & 0 & iJ & 0 & ig & ig \\ 0 & 0 & 0 & 0 & 0 & 0 & 0 & 0 & 0 & 0 & 0 & 0 & 1/\chi_{\hat{a}^\dagger\hat{b}} & 0 & iJ & 0 & iJ & 0 & -ig & -ig & 0 \\ 0 & 0 & 0 & 0 & 0 & 0 & 0 & 0 & 0 & 0 & 0 & 0 & 1/\chi_{\hat{a}^\dagger\hat{b}} & 0 & -iJ & 0 & -iJ & ig & 0 & 0 & ig \\ 0 & -ig & -ig & 0 & 0 & -ig & 0 & -ig & 0 & -iJ & 0 & -iJ & 0 & 1/\chi_{\hat{c}\hat{b}} & 0 & 2i\eta & 0 & 0 & 0 & 0 & 0 \\ 0 & ig & ig & 0 & 0 & 0 & ig & 0 & ig & 0 & iJ & 0 & iJ & 0 & 1/\chi_{\hat{c}\hat{b}}^* & 0 & -2i\eta & 0 & 0 & 0 & 0 \\ 0 & ig & -ig & 0 & 0 & ig & 0 & -ig & iJ & 0 & iJ & 0 & -2i\eta & 0 & 1/\chi_{\hat{c}\hat{b}}^* & 0 & 0 & 0 & 0 & 0 & 0 \\ 0 & -ig & ig & 0 & 0 & 0 & -ig & ig & 0 & 0 & -iJ & 0 & -iJ & 0 & 1/\chi_{\hat{c}\hat{b}}^* & 0 & 2i\eta & 0 & 0 & 0 & 0 \\ -iJ & 0 & -iJ & -iJ & 0 & 0 & 0 & -iJ & 0 & -ig & 0 & 0 & -ig & 0 & 0 & 0 & 0 & 1/\chi_{\hat{a}\hat{c}} & 0 & 0 & 2i\eta \\ iJ & 0 & iJ & 0 & iJ & 0 & 0 & 0 & iJ & 0 & ig & ig & 0 & 0 & 0 & 0 & 0 & 0 & 1/\chi_{\hat{a}\hat{c}}^* & -2i\eta & 0 \\ -iJ & 0 & iJ & 0 & -iJ & 0 & 0 & iJ & 0 & -ig & -ig & 0 & 0 & 0 & 0 & 0 & 0 & 0 & 2i\eta & 1/\chi_{\hat{a}^\dagger\hat{c}} & 0 \\ iJ & 0 & -iJ & iJ & 0 & 0 & 0 & 0 & -iJ & ig & 0 & 0 & ig & 0 & 0 & 0 & 0 & 0 & -2i\eta & 0 & 1/\chi_{\hat{a}^\dagger\hat{c}}^* \end{bmatrix}. \tag{B5}$$

Various susceptibilities are defined below.

$$\chi_{\hat{a}\hat{a}} = \frac{1}{2i\Delta_c - \kappa}, \tag{B6a}$$

$$\chi_{\hat{b}\hat{b}} = \frac{1}{-2i\omega_m - \gamma_m}, \tag{B6b}$$

$$\chi_{\hat{c}\hat{c}} = \frac{1}{2i\Delta_q - \Gamma - \Gamma_\phi}, \tag{B6c}$$

$$\chi_{\hat{a}\hat{b}} = \frac{1}{i(\Delta_c - \omega_m) - \frac{1}{2}(\kappa + \gamma_m)}, \tag{B6d}$$

$$\chi_{\hat{a}^\dagger\hat{b}} = \frac{1}{-i(\Delta_c + \omega_m) - \frac{1}{2}(\kappa + \gamma_m)}, \tag{B6e}$$

$$\chi_{\hat{c}\hat{b}} = \frac{1}{i(\Delta_q - \omega_m) - \frac{1}{2}(\Gamma + \frac{\Gamma_\phi}{2} + \gamma_m)}, \tag{B6f}$$

$$\chi_{\hat{c}^\dagger\hat{b}} = \frac{1}{-i(\Delta_q + \omega_m) - \frac{1}{2}(\Gamma + \frac{\Gamma_\phi}{2} + \gamma_m)}, \tag{B6g}$$

$$\chi_{\hat{a}\hat{c}} = \frac{1}{i(\Delta_c + \Delta_q) - \frac{1}{2}(\Gamma + \frac{\Gamma_\phi}{2} + \kappa)}, \tag{B6h}$$

$$\chi_{\hat{a}^\dagger\hat{c}} = \frac{1}{-i(\Delta_c - \Delta_q) - \frac{1}{2}(\Gamma + \frac{\Gamma_\phi}{2} + \kappa)}, \tag{B6i}$$

and  $\mathcal{N}$  is a column vector given by

$$\mathcal{N} = [n_c^i\kappa, n_m^i\gamma_m, n_q^i\Gamma, 0, 0, 0, 0, 2i\eta, -2i\eta, 0, 0, 0, 0, -ig, ig, 0, 0, -iJ, iJ, 0, 0]^T. \tag{B7}$$

The steady-state solution of the  $\mathbf{d}$  matrix can be written as

$$\mathbf{d} = -\mathcal{M}^{-1}\mathcal{N}. \tag{B8}$$

From Eq. (B8) we have calculated the final mechanical occupation  $n_f$  as a function of the device parameters. The plot of  $n_f$  as a function of coupling  $g$  and detuning ( $\tilde{\Delta}_q$ ) is shown in Fig. 3(d).

- [1] S. Barzanjeh, A. Xuereb, S. Gröblacher, M. Paternostro, C. A. Regal, and E. M. Weig, Optomechanics for quantum technologies, *Nat. Phys.* **18**, 15 (2022).
- [2] M. Aspelmeyer, T. J. Kippenberg, and F. Marquardt, Cavity optomechanics, *Rev. Mod. Phys.* **86**, 1391 (2014).
- [3] J. D. Teufel, T. Donner, D. Li, J. W. Harlow, M. S. Allman, K. Cicak, A. J. Sirois, J. D. Whittaker, K. W. Lehnert, and R. W. Simmonds, Sideband cooling of micromechanical motion to the quantum ground state, *Nature (London)* **475**, 359 (2011).
- [4] J. Chan, T. P. M. Alegre, A. H. Safavi-Naeini, J. T. Hill, A. Krause, S. Gröblacher, M. Aspelmeyer, and O. Painter, Laser cooling of a nanomechanical oscillator into its quantum ground state, *Nature (London)* **478**, 89 (2011).
- [5] E. E. Wollman, C. U. Lei, A. J. Weinstein, J. Suh, A. Kronwald, F. Marquardt, A. A. Clerk, and K. C. Schwab, Quantum squeezing of motion in a mechanical resonator, *Science* **349**, 952 (2015).
- [6] C. F. Ockeloen-Korppi, E. Damskäg, J.-M. Pirkkalainen, M. Asjad, A. A. Clerk, F. Massel, M. J. Woolley, and M. A. Sillanpää, Stabilized entanglement of massive mechanical oscillators, *Nature (London)* **556**, 478 (2018).
- [7] G. A. Peterson, S. Kotler, F. Lecocq, K. Cicak, X. Y. Jin, R. W. Simmonds, J. Aumentado, and J. D. Teufel, Ultrastrong Parametric Coupling between a Superconducting Cavity and a Mechanical Resonator, *Phys. Rev. Lett.* **123**, 247701 (2019).
- [8] S. Kotler, G. A. Peterson, E. Shojaei, F. Lecocq, K. Cicak, A. Kwiatkowski, S. Geller, S. Glancy, E. Knill, R. W. Simmonds, J. Aumentado, and J. D. Teufel, Direct observation of deterministic macroscopic entanglement, *Science* **372**, 622 (2021).
- [9] E. A. Wollack, A. Y. Cleland, R. G. Gruenke, Z. Wang, P. Arrangoiz-Arriola, and A. H. Safavi-Naeini, Quantum state preparation and tomography of entangled mechanical resonators, *Nature (London)* **604**, 463 (2022).
- [10] P. Rabl, Photon Blockade Effect in Optomechanical Systems, *Phys. Rev. Lett.* **107**, 063601 (2011).
- [11] A. Nunnenkamp, K. Børkje, and S. M. Girvin, Single-Photon Optomechanics, *Phys. Rev. Lett.* **107**, 063602 (2011).
- [12] P. Rabl, Cooling of mechanical motion with a two-level system: The high-temperature regime, *Phys. Rev. B* **82**, 165320 (2010).
- [13] Z.-L. Xiang, S. Ashhab, J. Q. You, and F. Nori, Hybrid quantum circuits: Superconducting circuits interacting with other quantum systems, *Rev. Mod. Phys.* **85**, 623 (2013).
- [14] A. A. Clerk, K. W. Lehnert, P. Bertet, J. R. Petta, and Y. Nakamura, Hybrid quantum systems with circuit quantum electrodynamics, *Nat. Phys.* **16**, 257 (2020).
- [15] I. Martin, A. Shnirman, L. Tian, and P. Zoller, Ground-state cooling of mechanical resonators, *Phys. Rev. B* **69**, 125339 (2004).
- [16] K. E. Khosla, M. R. Vanner, N. Ares, and E. A. Laird, Displacement Electromechanics: How to Detect Quantum Interference in a Nanomechanical Resonator, *Phys. Rev. X* **8**, 021052 (2018).
- [17] K. Jaehne, K. Hammerer, and M. Wallquist, Ground-state cooling of a nanomechanical resonator via a Cooper-pair box qubit, *New J. Phys.* **10**, 095019 (2008).
- [18] J. Hauss, A. Fedorov, S. André, V. Brosco, C. Hutter, R. Kothari, S. Yeshwanth, A. Shnirman, and G. Schön, Dissipation in circuit quantum electrodynamics: lasing and cooling of a low-frequency oscillator, *New J. Phys.* **10**, 095018 (2008).
- [19] Y.-D. Wang, Y. Li, F. Xue, C. Bruder, and K. Semba, Cooling a micromechanical resonator by quantum back-action from a noisy qubit, *Phys. Rev. B* **80**, 144508 (2009).
- [20] R. Nongthombam, A. Sahoo, and A. K. Sarma, Ground-state cooling of a mechanical oscillator via a hybrid electro-optomechanical system, *Phys. Rev. A* **104**, 023509 (2021).
- [21] X. Wang, A. Miranowicz, H.-R. Li, F.-L. Li, and F. Nori, Two-color electromagnetically induced transparency via modulated coupling between a mechanical resonator and a qubit, *Phys. Rev. A* **98**, 023821 (2018).
- [22] J. Manninen, M. T. Haque, D. Vitali, and P. Hakonen, Enhancement of the optomechanical coupling and Kerr nonlinearity using the Josephson capacitance of a Cooper-pair box, *Phys. Rev. B* **105**, 144508 (2022).
- [23] I. Wilson-Rae, P. Zoller, and A. Imamoglu, Laser Cooling of a Nanomechanical Resonator Mode to its Quantum Ground State, *Phys. Rev. Lett.* **92**, 075507 (2004).
- [24] P. Rabl, P. Cappellaro, M. V. Gurudev Dutt, L. Jiang, J. R. Maze, and M. D. Lukin, Strong magnetic coupling between an electronic spin qubit and a mechanical resonator, *Phys. Rev. B* **79**, 041302(R) (2009).
- [25] J.-M. Pirkkalainen, S. U. Cho, F. Massel, J. Tuorila, T. T. Heikkilä, P. J. Hakonen, and M. A. Sillanpää, Cavity optomechanics mediated by a quantum two-level system, *Nat. Commun.* **6**, 6981 (2015).
- [26] J.-M. Pirkkalainen, S. U. Cho, J. Li, G. S. Paroanu, P. J. Hakonen, and M. A. Sillanpää, Hybrid circuit cavity quantum electrodynamics with a micromechanical resonator, *Nature (London)* **494**, 211 (2013).
- [27] J. J. Viennot, X. Ma, and K. W. Lehnert, Phonon-Number-Sensitive Electromechanics, *Phys. Rev. Lett.* **121**, 183601 (2018).
- [28] I. C. Rodrigues, D. Bothner, and G. A. Steele, Coupling microwave photons to a mechanical resonator using quantum interference, *Nat. Commun.* **10**, 5359 (2019).
- [29] P. Schmidt, M. T. Amawi, S. Pogorzalek, F. Deppe, A. Marx, R. Gross, and H. Huebl, Sideband-resolved resonator electromechanics based on a nonlinear Josephson inductance probed on the single-photon level, *Commun. Phys.* **3**, 233 (2020).
- [30] D. Zoepfl, M. L. Juan, C. M. F. Schneider, and G. Kirchmair, Single-Photon Cooling in Microwave Magnetomechanics, *Phys. Rev. Lett.* **125**, 023601 (2020).
- [31] T. Bera, S. Majumder, S. K. Sahu, and V. Singh, Large flux-mediated coupling in hybrid electromechanical system with a transmon qubit, *Commun. Phys.* **4**, 12 (2021).
- [32] A. D. O'Connell, M. Hofheinz, M. Ansmann, R. C. Bialczak, M. Lenander, E. Lucero, M. Neeley, D. Sank, H. Wang, M. Weides, J. Wenner, J. M. Martinis, and A. N. Cleland, Quantum ground state and single-phonon control of a mechanical resonator, *Nature (London)* **464**, 697 (2010).
- [33] P. Arrangoiz-Arriola, E. A. Wollack, Z. Wang, M. Pechal, W. Jiang, T. P. McKenna, J. D. Witmer, R. Van Laer, and A. H. Safavi-Naeini, Resolving the energy levels of a nanomechanical oscillator, *Nature (London)* **571**, 537 (2019).
- [34] D. Bothner, I. C. Rodrigues, and G. A. Steele, Four-wave-cooling to the single phonon level in Kerr optomechanics, *Commun. Phys.* **5**, 33 (2022).
- [35] T. Luschmann, P. Schmidt, F. Deppe, A. Marx, A. Sanchez, R. Gross, and H. Huebl, Mechanical frequency control in induc-

- tively coupled electromechanical systems, [Sci. Rep. 12, 1608 \(2022\)](#).
- [36] J. Gambetta, A. Blais, D. I. Schuster, A. Wallraff, L. Frunzio, J. Majer, M. H. Devoret, S. M. Girvin, and R. J. Schoelkopf, Qubit-photon interactions in a cavity: Measurement-induced dephasing and number splitting, [Phys. Rev. A 74, 042318 \(2006\)](#).
- [37] A. Blais, A. L. Grimsmo, S. M. Girvin, and A. Wallraff, Circuit quantum electrodynamics, [Rev. Mod. Phys. 93, 025005 \(2021\)](#).
- [38] P. Zhang, Y. D. Wang, and C. P. Sun, Cooling Mechanism for a Nanomechanical Resonator by Periodic Coupling to a Cooper Pair Box, [Phys. Rev. Lett. 95, 097204 \(2005\)](#).
- [39] M. Kounalakis, Y. M. Blanter, and G. A. Steele, Flux-mediated optomechanics with a transmon qubit in the single-photon ultrastrong-coupling regime, [Phys. Rev. Res. 2, 023335 \(2020\)](#).
- [40] C. W. Gardiner and P. Zoller, *Quantum Noise*, Springer Series in Synergetics (Springer Berlin, Heidelberg, 2004).
- [41] G. Lindblad, On the generators of quantum dynamical semi-groups, [Commun. Math. Phys. 48, 119 \(1976\)](#).
- [42] J. Krause, C. Dickel, E. Vaal, M. Vielmetter, J. Feng, R. Bounds, G. Catelani, J. M. Fink, and Y. Ando, Magnetic Field Resilience of Three-Dimensional Transmons with Thin-Film AlAlO<sub>x</sub>/Al Josephson Junctions Approaching 1 T, [Phys. Rev. Appl. 17, 034032 \(2022\)](#).
- [43] P. Forn-Díaz, L. Lamata, E. Rico, J. Kono, and E. Solano, Ultrastrong coupling regimes of light-matter interaction, [Rev. Mod. Phys. 91, 025005 \(2019\)](#).